CHEMISTRY OF MATERIALS

Article

Cite This: Chem. Mater. 2019, 31, 2182−2190

pubs.acs.org/cm

Fully Inorganic Ruddlesden−Popper Double Cl−I and Triple Cl−Br−I Lead Halide Perovskite Nanocrystals

Quinten A. Akkerman,[†,‡] Eva Bladt,[§] Urko Petralanda,[†] Zhiya Dang,[†] Emanuela Sartori,[‡] Dmitry Baranov,[†] Ahmed L. Abdelhady,[†] Ivan Infante,[*,†,∥] Sara Bals,[*,§] and Liberato Manna[*,†]

[†]Nanochemistry Department, Istituto Italiano di Tecnologia, Via Morego 30, 16163 Genova, Italy

[‡]Dipartimento di Chimica e Chimica Industriale, Università degli Studi di Genova, Via Dodecaneso, 31, 16146 Genova, Italy

[§]EMAT, Department of Physics, University of Antwerpen, Groenenborgerlaan 171, 2020 Antwerpen, Belgium

[∥]Department of Theoretical Chemistry, Faculty of Science, Vrije Universiteit Amsterdam, de Boelelaan 1083, 1081 HV Amsterdam, The Netherlands

Supporting Information

ABSTRACT: The vast majority of lead halide perovskite (LHP) nanocrystals (NCs) are currently based on either a single halide composition ($CsPbCl_3$, $CsPbBr_3$, and $CsPbI_3$) or an alloyed mixture of bromide with either Cl^- or I^- [i.e., $CsPb(Br:Cl)_3$ or $CsPb(Br:I)_3$]. In this work, we present the synthesis as well as a detailed optical and structural study of two halide alloying cases that have not previously been reported for LHP NCs: $Cs_2PbI_2Cl_2$ NCs and triple halide $CsPb(Cl:Br:I)_3$ NCs. In the case of $Cs_2PbI_2Cl_2$, we observe for the first time NCs with a fully inorganic Ruddlesden−Popper phase (RPP) crystal structure. Unlike the well-explored organic−inorganic RPP, here, the RPP formation is triggered by the size difference between the halide ions. These NCs exhibit a strong excitonic absorption, albeit with a weak photoluminescence quantum yield (PLQY). In the case of the triple halide $CsPb(Cl:Br:I)_3$ composition, the NCs comprise a $CsPbBr_2Cl$ perovskite crystal lattice with only a small amount of incorporated iodide, which segregates at RPP planes' interfaces within the $CsPb(Cl:Br:I)_3$ NCs. Supported by density functional theory calculations and postsynthetic surface treatments to enhance the PLQY, we show that the combination of iodide segregation and defective RPP interfaces are most likely linked to the strong PL quenching observed in these nanostructures. In summary, this work demonstrates the limits of halide alloying in LHP NCs because a mixture that contains halide ions of very different sizes leads to the formation of defective RPP interfaces and a severe quenching of LHP NC's optical properties.

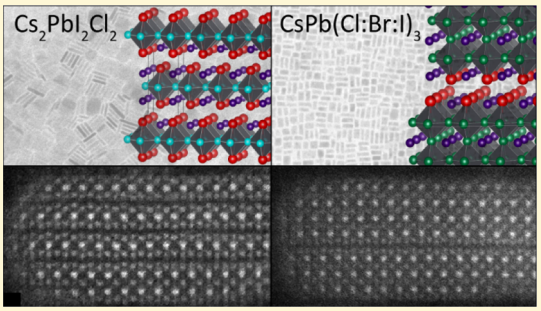

Over the past decade, lead halide perovskites (LHPs) have gained much interest in the materials science community owing to their outstanding optoelectronic properties.[1] More recently, research has also expanded to include studies on colloidal LHP nanocrystals (NCs), especially cesium-based ones ($CsPbX_3$, with X = Cl, Br, I).[2] This has resulted in the successful synthesis of NC samples with tunable compositions, great control over their size and shape, and the fabrication of several different types of LHP NC-based devices.[3] One striking feature of LHP NCs is that they are easy to alloy and dope with other elements, which either improves their optical properties or causes a down-converted emission. For instance, several groups have extended the synthesis of LHP NCs to quaternary compositions, such as $[Cs:FA]PbI_3$ (in which FA = formamidinium), $CsPb[Br:X]_3$, or $Cs[Pb:M]X_3$ (in which M = Sr^{2+}, Sn^{2+}, Mn^{2+}, Ni^{2+}, etc.), and even quinary compositions such as $[Cs:FA]Pb[Br:I]_3$.[4−12] Of all these alloyed compositions, the most investigated ones are those in which two different types of halides are present (namely, Br/Cl or Br/I). These halides can be mixed in the structure at any possible Br/Cl or Br/I ratio, which allows the band gap to be precisely tuned from about 400−700 nm.[2,13,14] As is the case in bulk LHPs, mixing Br^- with either Cl^- or I^- anions results in homogenous alloys with a well-defined band gap and narrow PL peak. The formation of homogenous alloys is made possible by small variations in the length of the ionic radius, which only decreases by 8% going from Br^- to Cl^- and increases by 12% from Br^- to I^-. On the other hand, the difference in the length of the ionic radii between Cl^- and I^- is apparently too big (19%) to permit homogenous mixing.[15] In the case of $CsPbI_3$ NCs, the alloying with Cl^- is limited to only a few percent.[12,16,17] Interestingly, the incorporation of a small amount of Cl^- into $MAPbI_3$ (in which MA = methylammonium) thin films or $CsPbI_3$ NCs has been found to be beneficial in terms of increasing long-term stability and improving the optical properties.[16,18] There have not been

Received: February 1, 2019
Revised: March 1, 2019
Published: March 4, 2019

DOI: 10.1021/acs.chemmater.9b00489
Chem. Mater. 2019, 31, 2182−2190

any studies on mixing all three halides in LHP NCs, and there have only been few works on the bulk.[19]

Here, we have synthesized and studied two types of halide mixing that have not previously been reported for NCs; $Cs_2PbI_2Cl_2$ NCs with a Cl/I feed ratio of 1:1 and $CsPb(Cl:Br:I)_3$ NCs with a Cl/Br/I feed ratio of 1:1:1. In both these cases, the synthesized NCs are nanoplatelet-shaped. In the case of $Cs_2PbI_2Cl_2$, the NCs crystallize into a Ruddlesden−Popper phase (RPP), matching that of previously investigated bulk $Cs_2PbI_2Cl_2$.[20] Even though these NCs are relatively big (5 nm thick by 40 nm in the lateral dimensions), they exhibit an extremely confined excitonic absorption as a result of the individually separated Pb−Cl layers within the RPP. When the Cl/Br/I halides are mixed in a 1:1:1 ratio, perovskite NCs with an optical absorption and crystal lattice similar to those of $CsPbBr_2Cl$ NCs are obtained, and only a small amount of I^- is incorporated into the NCs, as was confirmed by elemental analysis. These triple halide NCs, however, have a very poor photoluminescence quantum yield (PLQY, well below 1%), which is significantly lower than that of $CsPbBr_2Cl$ NCs. By means of high-resolution high-angle annular scanning transmission electron microscopy (HAADF-STEM) analysis, it was found that the $CsPb(Cl:Br:I)_3$ NCs predominantly crystallize in a perovskite crystal structure, but they contain several planar defects which could be identified as RPP planes. By combining a quantitative high-resolution HAADF-STEM analysis with density functional theory (DFT) calculations, we confirmed that the iodide anions are segregated from the pure LHP structure. Subsequently, they migrate to the RPP interface, forming RPP planes.

EXPERIMENTAL SECTION

Chemicals. Cesium carbonate (Cs_2CO_3, 99%), lead(II) chloride ($PbCl_2$, 98% trace metals basis), lead(II) bromide ($PbBr_2$, 99.999% trace metal basis), lead(II) iodide (PbI_2, 99.999% trace metal basis), ammonium thiocyanate (ATCN, 97.5%), oleylamine (OLAM, 98%), oleic acid (OA, 90%), 1-octadecene (ODE, 90%), and toluene (TOL, anhydrous, 99.8%) were purchased from Sigma-Aldrich. All chemicals were used as received, without any further purification.

Synthesis of $Cs_2PbI_2Cl_2$, $CsPb(Cl:Br:I)_3$, $CsPbCBr_2Cl$, and $CsPbCl_3$ NCs. The $Cs_2PbI_2Cl_2$, $CsPb(Cl:Br:I)_3$, $CsPbCBr_2Cl$, and $CsPbCl_3$ NCs were synthesized based on a hot plate synthesis that had previously been used to prepare Cs_4PbX_6 and $CsPbBr_3$ NCs.[21,22] All syntheses were performed in air and without any predried chemicals or solvents. In a typical synthesis, PbX_2 salts (in total 0.2 mmol, with 1:1 $PbCl_2/PbI_2$ for $Cs_2PbI_2Cl_2$, 1:1:1 $PbCl_2/PbBr_2/PbI_2$ for $CsPb(Cl:Br:I)_3$, and 1:2 $PbCl_2/PbBr_2$ for $CsPbBr_2Cl$) were dissolved in 5 mL ODE, 0.125 mL OA, and 0.5 mL OLAM in a 20 mL vial on a hot plate set at 250 °C. When the temperature reached 185 °C (for $CsPb(Cl:Br:I)_3$ and $CsPbBr_2Cl$) or 165 °C (for $Cs_2PbI_2Cl_2$), 0.5 mL of Cs−OA (0.4 g Cs_2CO_3 dissolved in 15 mL ODE and 1.75 mL OA at 150 °C) was swiftly injected, and the reaction was quickly cooled down with a cold water bath. The NCs were directly washed via centrifugation (at 6000 rpm for 10 min), followed by redispersion in 5 mL TOL. For high-resolution transmission electron microscopy (HRTEM) and X-ray diffraction (XRD), the NCs were rinsed several times with TOL, as previously reported.[23]

Transmission Electron Microscopy. Conventional TEM images were acquired on a JEOL JEM-1011 microscope equipped with a thermionic gun at an accelerating voltage of 100 kV. The samples were prepared by drop-casting diluted NC solutions onto 200 mesh carbon-coated copper grids.

Energy-Dispersive Spectroscopy. STEM-EDS was performed on a JEOL JEM-2200FS microscope equipped with a Schottky emitter operating at 200 kV, a CEOS spherical aberration corrector for the objective lens, an in-column energy filter (Omega-type), and a Bruker Quantax 400 EDS system with an XFlash 5060 detector.

High-Resolution High-Angle Annular Dark-Field Imaging Scanning Transmission Electron Microscopy. High-resolution HAADF-STEM images were acquired using a cubed FEI Titan microscope operating at 300 kV. A probe semiconvergence angle of ∼20 mrad was used. The quantitative HAADF-STEM analysis was performed using StatSTEM.[24] The intensity values of the halide-containing atomic columns are calculated by fitting a Gaussian function to each individual column. The intensity value equals the volume of the Gaussian peak.

Powder XRD Analysis. XRD patterns were obtained using a PANalytical Empyrean X-ray diffractometer equipped with a 1.8 kW Cu Kα ceramic X-ray tube and a PIXcel3D 2 × 2 area detector operating at 45 kV and 40 mA. The diffraction patterns were collected in air at room temperature using parallel-beam geometry and symmetric reflection mode. All XRD samples were prepared by drop-casting a concentrated solution on a zero diffraction quartz wafer.

Steady-State Absorbance, Photoluminescence, and Photoluminescence Excitation Spectra. Absorbance spectra from solutions of NCs were recorded using a Cary-300 spectrophotometer. The photoluminescence (PL) and PL excitation (PLE) spectra were recorded using a FLS920 Edinburgh Instruments spectrofluorimeter. Concentrated NC solutions were diluted with TOL in 4 mm × 10 mm quartz cuvettes, as described below.

PLQY Measurements. The PLQYs of as-synthesized and thiocyanate-treated $CsPbBr_2Cl$ and $CsPb(Cl:Br:I)_3$ NCs were measured on freshly made samples using a FLS920 Edinburgh Instruments spectrofluorimeter equipped with an integrating sphere. The samples for PLQY were prepared in air by diluting 13−25 μL of the concentrated NC solutions with 1 mL of anhydrous TOL in 4 mm × 10 mm quartz cuvettes capped with white PTFE stoppers (Hellma-Analytics, part number 114F-10-40). Dilutions were performed shortly before the measurements. The samples were excited at 350 nm using the xenon lamp (Xe900) with an excitation slit width set at 10 nm. The emission slit width was set at 0.40 nm. The cuvettes were oriented inside the sphere such that the excitation was through the 4 mm path length. The photon number spectra for the samples and TOL solvent reference were collected over the 325−550 nm spectral range with a step size of 1 nm, and a dwell time of 0.2 s per step. Five consecutive scans were added together to obtain the data for PLQY calculations. Corrections for the background, PMT detector sensitivity, and the lamp reference detector were applied automatically during the data collection by the software. For PLQY calculations, the photon number spectra were integrated in the range of 335−365 nm in order to determine the total number of scattered photons (sc photons), and in the ranges 435−550 nm ($CsPbBr_2Cl$) or 435−500 nm [$CsPb(Cl:Br:I)_3$] to determine the total number of emitted photons (em photons). The values of PLQY were calculated using the following formula: PLQY, % = $100 \times (N^{\text{sample}}_{\text{em photons}} - N^{\text{reference}}_{\text{em photons}})/(N^{\text{reference}}_{\text{sc photons}} - N^{\text{sample}}_{\text{sc photons}})$ and reported without correction for self-absorption. We attempted to measure PLQY of $Cs_2PbI_2Cl_2$ NCs using 385 nm excitation, but the sample emission was too low, indicating that PLQY of the sample was much smaller than 0.1%. The PLQY results are summarized in Table S1.

PL Lifetime Measurements. Time-dependent PL intensity decays were measured after the PLQY measurements on the same samples using the time-correlated single-photon counting technique using a FLS920 Edinburgh Instruments spectrofluorimeter. The PL intensity decay curves are shown on a logarithmic scale. The samples were excited with a 401.2 nm picosecond pulsed diode laser (EPL-405, Edinburgh Instruments) and a 500 ns pulse period. The PL decays were collected at the peak of the emission spectra with an emission slit width of 3−5 nm.

DFT Calculations. All DFT calculations were performed using the CP2K quantum chemistry code,[25] employing the Perdew-Burke-Ernzerhof (PBE) exchange−correlation functional and double ζ basis set plus polarization functions.[26,27] Scalar relativistic effects have been incorporated with an effective core potential, while spin−orbit

DOI: 10.1021/acs.chemmater.9b00489
Chem. Mater. 2019, 31, 2182−2190

coupling effects were not added in the calculations. Charge-balanced NC models were built according to previous receipt from some of us.[28−30] Time-dependent calculations were carried out using the simplified Tamm−Dancoff approach that allows the simultaneous computation of hundredths of excited states.[31] This methodology has been implemented within the QMflows-namd software package and is suitable to compute the optical absorption spectrum of the mixed lead halide model systems until approximately 4.0 eV.[32]

RESULTS AND DISCUSSION

The $Cs_2PbI_2Cl_2$ and $CsPb(Cl:Br:I)_3$ NCs were synthesized based on the previously reported synthesis of $CsPbBr_3$ NC.[21] Here, a Cs−oleate solution was injected into a solution of ODE, OLAM, and OA containing either 1:1 $PbCl_2/PbI_2$ or 1:1:1 $PbCl_2/PbBr_2/PbI_2$ (see the Supporting Information, for more details). In the case of a 1:1 ratio of $PbCl_2/PbI_2$, NCs that were about 4.2 ± 0.6 nm thick and 21 ± 3 nm wide were produced, as is shown in Figure 1a. As depicted in Figure 1b,

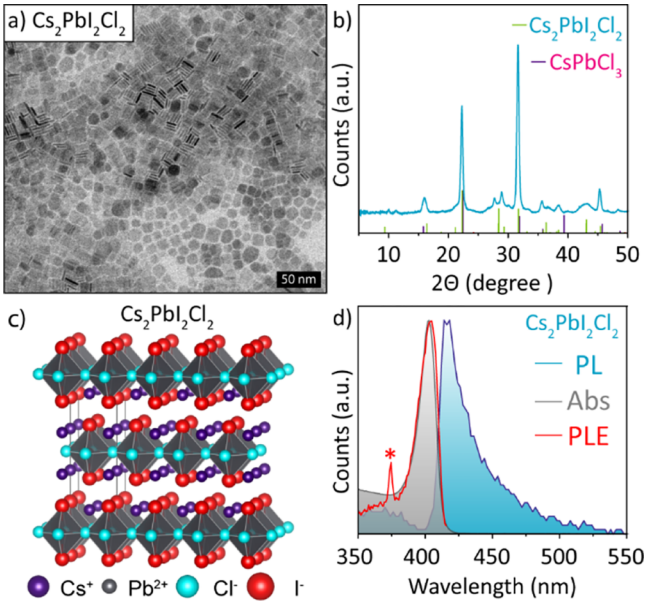

Figure 1. Optical and structural data of $Cs_2PbI_2Cl_2$ NCs. (a) TEM image of monodisperse $Cs_2PbI_2Cl_2$ NCs. (b) XRD pattern of $Cs_2PbI_2Cl_2$ NCs matching that of bulk $Cs_2PbI_2Cl_2$. (c) Crystal structure of $Cs_2PbI_2Cl_2$ RPP. (d) Strong excitonic absorption from $Cs_2PbI_2Cl_2$ and broad PL of $Cs_2PbI_2Cl_2$ NCs. PLE spectra of $Cs_2PbI_2Cl_2$ NCs (red line, recorded at 411 nm) overlapping with the absorption spectrum, indicating that the PL originates from $Cs_2PbI_2Cl_2$. The asterisk marks the instrumental artifact. XRD reference patterns correspond to ref 20.

these NCs crystallized in the RPP $Cs_2PbI_2Cl_2$ phase (K_2NiF_4-type phase), which consists of corner-sharing $[PbI_2Cl_4]^{4-}$ octahedra layers. In the $Cs_2PbI_2Cl_2$ phase, the Cl^- ions occupy the equatorial halide sites and the I^- ions occupy the axial halide sites, as is depicted in Figure 1c.[20] Although the $Cs_2PbI_2Cl_2$ crystal lattice shares similar diffraction peaks with the $CsPbCl_3$ crystal lattice, it has several additional peaks, as is demonstrated in Figure S1a. Furthermore, because of the breaking of symmetry in the z direction of the lattice, the diffraction from the {112} family of planes normally observed in $CsPbCl_3$ cannot be observed in the $Cs_2PbI_2Cl_2$ XRD pattern. As will be further discussed later on, the XRD pattern also confirmed that the NCs grow anisotropically, as several peaks, notably those of the {xy0} plane family are significantly sharper than the other diffraction peaks. This further indicates that the NCs are essentially formed by stacked layers of corner-sharing $[PbI_2Cl_4]^{4-}$ octahedra which are charge-balanced by Cs^+ counterions. The strong confinement of carriers inside these single layers of lead chloride perovskites is also evident from the optical absorption spectrum, which is presented in Figure 1d. Here, the $Cs_2PbI_2Cl_2$ NCs exhibit a narrow excitonic absorption around 400 nm (3.1 eV), which matches a band gap of 3.04 eV that was reported by Kanatzidis' group.[20] This is a sharper absorption than that of $CsPbCl_3$ NCs (Figure S1b). However, the PL of the $Cs_2PbI_2Cl_2$ NCs is significantly broader than that of $CsPbCl_3$ NCs, and it exhibits a broad tail that is similar to what has been reported previously (Figure 1d).[20] This broad PL was too weak to determine a PLQY, but the PLE, which is shown in Figures 1d and S2, matches the absorption, indicating that the broad asymmetric PL indeed originates from the $Cs_2PbI_2Cl_2$ NCs.

It is important to stress that, from the structural point of view, these "all-inorganic" RPP $Cs_2PbI_2Cl_2$ NCs are very different from the previously reported organic−inorganic RPPs (including organic−inorganic RPP NCs), in which bulky organic ligands act as spacers between the stacked lead halide layers [such as $(BA)_2(MA)_{n-1}Pb_nI_{3n+1}$, with BA = butylammonium].[33−36] In our RPP $Cs_2PbI_2Cl_2$ NCs, the individual layers are not separated by bulky ligands (acting as cations) but rather by the large size difference of the Cl^- and I^- anions. Therefore, their periodicity along the stacking direction is much smaller than that of the organic−inorganic RPP phase. As a consequence, we do not observe low-angle XRD diffractions, originating from large periodicities along the stacking direction (Figure 1b).[37−39] Our all-inorganic RPP $Cs_2PbI_2Cl_2$ NCs are also different from the ligand-passivated ultrathin two-dimensional LHP NCs (nanosheets and nanoplatelets), which can have thickness down to a few unit cells and thus can exhibit superstructure effects at low diffraction angles which arise from the stacking of the ligand-coated nanosheets on top of each other.[37−40] The $Cs_2PbI_2Cl_2$ NCs, even though they are coated with organic ligands, are too thick for such periodicities to be appreciated by low-angle XRD diffraction (see again Figure 1b). Finally, because the individual layers in these $Cs_2PbI_2Cl_2$ NCs are not separated by bulky ligands, the NCs are expected to have an electronic structure and optical properties that are significantly different from those of the organic−inorganic RPPs and of the ligand-coated ultrathin LHP nanosheets.

The crystal structure of the $Cs_2PbI_2Cl_2$ NCs was further studied via high-resolution HAADF-STEM imaging. The $Cs_2PbI_2Cl_2$ NCs were observed while they were lying parallel to the substrate, as can be seen in Figure 2a. Here, only slight differences in the intensities were found throughout the nanostructure, which is similar to previous findings in HRTEM studies on RPP domains in $CsPbBr_3$.[41] These intensities can be understood by observing such a NC from the side, as is depicted in Figure 2b because it consists of alternating RPP layers. Such alternating RPP domains result in atomic rows that contain both Cs and Pb, which is not the case for perovskite structures. Because of Cs and Pb mixing in one atomic row, which can be observed in Figure 2b, no distinct intensity differences are present in the atomic columns in Figure 2a. Although no clear proof of the coexistence of $CsPbCl_3$ was found in the XRD patterns of the $Cs_2PbI_2Cl_2$ NCs, the NCs did not solely consist of single layers of $Cs_2PbI_2Cl_2$. Indeed, they also displayed several bilayers of

DOI: 10.1021/acs.chemmater.9b00489
Chem. Mater. 2019, 31, 2182−2190

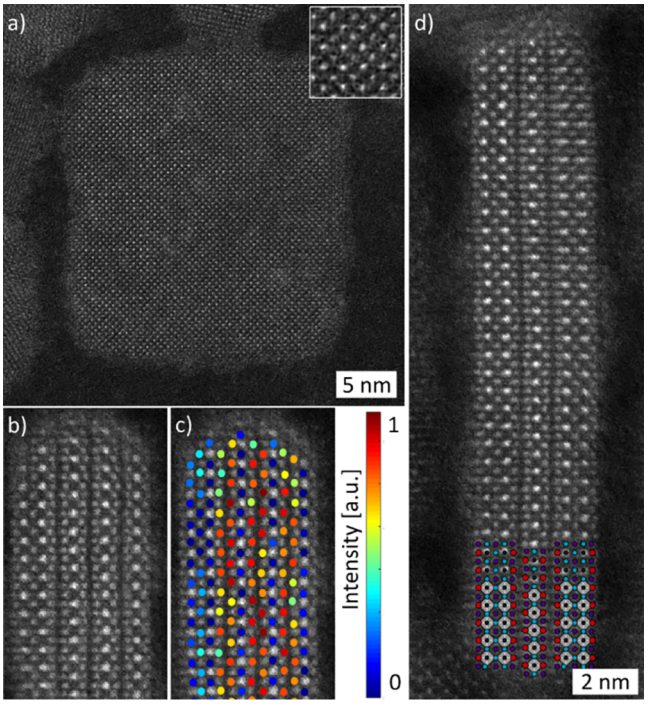

Figure 2. HAADF-STEM analysis of $Cs_2PbI_2Cl_2$ NCs. (a) Top view of a $Cs_2PbI_2Cl_2$ NC that is parallel to the substrate, within the inset, a highlight of the atomic arrangement. (b) Side view of a $Cs_2PbI_2Cl_2$ NC, which clearly matches the alternating layers of the RPP. (c) Volume of the fitted Gaussian peaks of the halide columns of the NC as shown in Figure 2b. The significant increase in the intensity values measured at the axial positions matches the excepted iodide positions. (d) $Cs_2PbI_2Cl_2$ NC observed perpendicular to the substrate overlaid with the crystal structure of $Cs_2PbCl_2I_2$ (Cs^+ = purple, Pb^{2+} = black, Cl^- = blue, I^- = red, and $[PbI_2Cl_4]^{4-}$ octahedra = gray), indicating a single layer of $Cs_2PbI_2Cl_2$ in between two bilayers of $Cs_3Pb_2I_2Cl_5$. For additional HAADF-STEM data, see Figures S3 and S4.

$Cs_3Pb_2I_2Cl_5$ (see the bottom part of Figures 2d as well as S3a–c).

To further prove that the I^- ions occupy the axial halide sites, and that the Cl^- ions occupy the equatorial (perovskite) halide sites (see Figure 1c), we performed a quantitative high-resolution HAADF-STEM analysis. Using StatSTEM,[24] we calculated the intensities of the halide atomic columns by fitting a Gaussian function to each individual atomic column consisting of only halides. In Figures 2c and S4, the intensity values, that is, the volume of each fitted Gaussian peak, are plotted, and the results indicate that the columns at the planar defect have a higher intensity than the columns in the NC's bulk. Because the intensity in an HAADF-STEM image scales with the thickness of the sample and the atomic number of the present elements and the NCs have a constant thickness, this could certainly indicate that more iodine is present in the columns that are located at the RPP. The halide columns between the Pb columns, on the other hand, clearly have a lower intensity value (Figure 2c), which suggests the presence of Cl in these columns because Cl has a lower atomic number than I (Z_{Cl} = 17 and Z_I = 53). Because of this low atomic number, the atomic columns are not visible in HAADF-STEM images (Figure 2b,d). Figure 2d shows a $Cs_2PbI_2Cl_2$ NC that is overlaid with a model of alternating RPP layers, which is based on the quantitative HAADF-STEM results (purple: Cs^+, black: Pb^{2+}, blue: Cl^-, and red: I^-). Usually, energy-dispersive X-ray spectroscopy (EDS) can be used to retrieve compositional information. However, because of the high sensitivity of the NCs to the electron beam in this case, an atomic resolution EDS map with a sufficient signal-to-noise ratio cannot be acquired before any damage has occurred.

For the second type of halide alloying that we investigated, we used all three halides (Cl, Br, and I) in the synthesis of LHP NCs. As is shown in Figure 3a, this combination resulted in

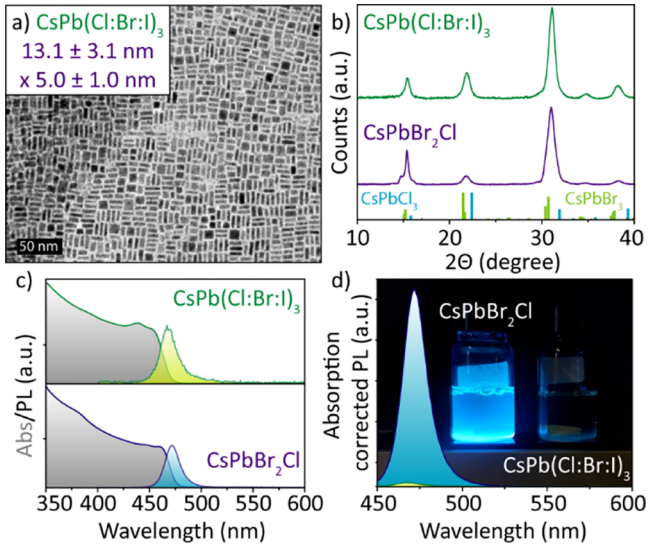

Figure 3. Overview of structural and optical data of $CsPb(Cl:Br:I)_3$ NCs. (a) TEM image of $CsPb(Cl:Br:I)_3$ NCs. (b) XRD pattern of $CsPb(Cl:Br:I)_3$ NCs that matches that of $CsPbBr_2Cl$ NCs. (c) Optical properties of $CsPb(Cl:Br:I)_3$ NCs, evidencing an absorption edge at around 460 nm and a weak but narrow emission around 470 nm, matching the same band gap of $CsPbBr_2Cl$ NCs. (d) Absorption-corrected PL of $CsPb(Cl:Br:I)_3$ NCs compared to brightly emitting $CsPbBr_2Cl$ NCs, with a photo of $CsPbBr_2Cl$ and $CsPb(Cl:Br:I)_3$ NCs under UV excitation, showing no visible PL for the $CsPb(Cl:Br:I)_3$ NCs. $CsPbCl_3$ (cubic) and $CsPbBr_3$ (orthorhombic) XRD reference patterns correspond to 98-002-9076 and 96-451-0746.

NCs with lateral dimensions of approximately 13 nm and thicknesses of about 5 nm. Different to the $Cs_2PbI_2Cl_2$ NCs, the $CsPb(Cl:Br:I)_3$ NCs crystallized in the perovskite crystal lattice, with a lattice spacing of about 5.8 Å, which matches that of $CsPbBr_2Cl$ NCs (see Figures 3b and S5). Furthermore, the $CsPb(Cl:Br:I)_3$ NCs have an absorption edge (around 460 nm) and PL peak (around 470 nm) that are similar to those of $CsPbBr_2Cl$ NCs (Figure 3c). Interestingly, the mixed $CsPb(Cl:Br:I)_3$ NCs hardly exhibited any visible PL, which is in stark contrast to the $CsPbBr_2Cl$ NCs' bright emission (Figure 3d). Indeed, the $CsPb(Cl:Br:I)_3$ NCs exhibited a measurable PLQY of about 0.1% (see Figure S6), which is about 50 times lower than that of the $CsPbBr_2Cl$, which has a PLQY of 5.5%. These findings are in agreement with those that have been previously reported for untreated $CsPb(Br:Cl)_3$ NCs.[42] Contrary to the 1:1:1 Cl/Br/I feed ratio that is used in during the synthesis of the NCs, the final elemental Cl/Br/I ratio, which was measured with EDS, was found to be 1:1.7:0.3. This again matches the optical absorption, as well as the crystal lattice, which is closer to that of 2:1 Br/Cl than that of the larger $CsPbI_3$ unit cell.

To further study the crystal lattice of these $CsPb(Cl:Br:I)_3$ NCs, and to further understand why their PLQY is so low, we

DOI: 10.1021/acs.chemmater.9b00489
Chem. Mater. 2019, 31, 2182–2190

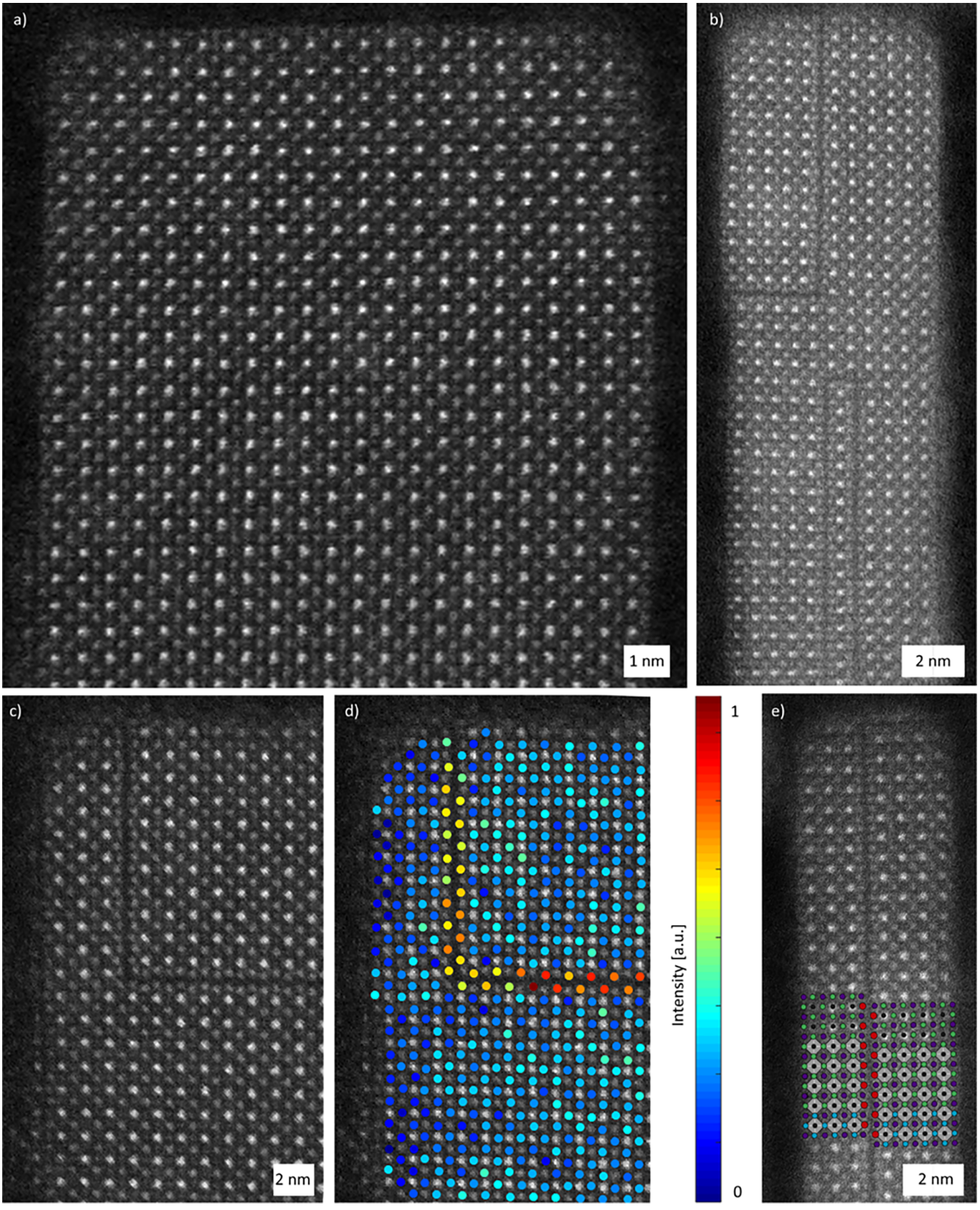

Figure 4. HAADF-STEM analysis of $Cs(Cl:Br:I)_3$ NCs. HAADF-STEM images of $Cs(Cl:Br:I)_3$ NCs, showing (a) the perovskite lattice and (b,c) NCs with several plane shifts. (d) Volume of the fitted Gaussian peaks of the halide columns of the NC as shown in (c) indicates increased intensity values of the halide columns around the RPP planes, confirming an increased concentration of iodide ions at these positions. (e) RPP plane shift model (Cs^+ = purple, Pb^{2+} = black, Cl^-/Br^- = blue, I^- = red, and PbX_6 octahedra = gray) overlapping an HAADF-STEM image of a $CsPb(Cl:Br:I)_3$ NC. For additional HAADF-STEM data, see Figures S7−S9.

DOI: 10.1021/acs.chemmater.9b00489
Chem. Mater. 2019, 31, 2182−2190

performed a high-resolution HAADF-STEM analysis. As is reported in Figure 4a, the $CsPb(Cl:Br:I)_3$ NCs consist predominantly of a perovskite crystal structure with a lattice spacing of (5.9 ± 0.1) Å, which is in agreement with the XRD measurements. Large grain boundaries were observed in many of the $CsPb(Cl:Br:I)_3$ NCs, as is shown in Figures 4b and S7. These grain boundaries are made of shifted lattices over half of the unit cell along the [100] planes. These types of lattice shifts are similar to those of the $Cs_2PbI_2Cl_2$ RPP NCs but consist of only a single-shifted plane between two layers of 3D perovskites.[35,36,41,43] Interestingly, many of the NCs contained multiple RPP planes, resulting in corners, zigzags, single layers of RPPs, and double layers of RPPs (see Figures 4b and S7). These RRP planes are mostly present in only one part of the NC, and not throughout the whole NC, which explains why the overall crystal lattice is still observed as a perovskite lattice. These types of RPP plane shifts have been observed in pure $CsPbBr_3$ NCs before, but they originated from a post synthesis chemical fusion of the NCs.[44,45]

In some cases, the formation of RPP planes can also be observed from the [001] direction, as can be seen in Figure S8. If the lattice shift is located in the middle of the NCs, half of the crystal is shifted, which leads to mixed Pb and Cs atomic columns with equal amounts of Pb and Cs throughout the atomic columns. Thus, the RPP shift results in averaging of the Pb and Cs intensities in the Pb- and Cs-containing columns, which leads to comparable intensity values because not all-Cs or all-Pb atomic columns are present. This was observed for several NCs, which exhibited regions which did not show separate different intensities for Pb−X and Cs columns but rather only columns with a comparable intensity. This is not caused by the alternating layers of a RPP, as is shown in Figure 2b,d but by a single RPP plane shift. The same was observed in large $CsPbBr_3$ nanosheets, which sometimes contained RPP domains.[41] Because the iodide ions tend to occupy the axial halide positions in the RPP $Cs_2PbI_2Cl_2$ phase, it is likely that the small amount of incorporated iodine species in the $CsPb(Cl:Br:I)_3$ NCs are segregated at the RPP halide positions. To confirm that the iodide halides segregate at the RPP, we again performed a quantitative high-resolution HAADF-STEM analysis to investigate the intensities of the halide columns using StatSTEM, and we found that all the halide columns that are directly positioned in the RPP exhibit significantly higher intensities compared to those outside the RPP planes (see Figures 4c,d and S9). This indicates that the iodide halides do tend to segregate into the RPP planes. This is in accordance with the small amount of iodide that was observed in the elemental analysis, but the NCs generally have the same properties as $CsPbBr_2Cl$ NCs.

To identify whether the PL quenching originates from the presence of RPP planes in the inorganic cores of the $CsPb(Cl:Br:I)_3$ NCs, or is mainly related to surface trapping effects, the NCs were subjected to a surface treatment that is generally known to increase the PL by passivating surface traps.[30,46,47] The addition of ATCN[46] increased the PLQY of the $CsPbBr_2Cl$ NCs by almost a factor of 6, from 5.5 to 33.1%, as is shown in Figures S6 and S11. The PL lifetime of thiocyanate-treated $CsPbBr_2Cl$ NCs was characterized by a slower decay at early times (~0−30 ns) and a faster decay at longer times (~30−200 ns) compared to untreated NCs, similar to the prior reports (Figure S12).[42,46,48] The same treatment on the $CsPb(Cl:Br:I)_3$ NCs resulted in an overall faster PL decay of the treated NCs compared to untreated NCs (Figures S11 and S13), however with no significant enhancement of the PLQY (see Figure S11). Overall, these experiments indicate that the low PLQY cannot stem solely from surface trapping effects and therefore must also be due to the presence of RPP planes in the core of the NCs that are not accessible by postsynthesis surface treatments.

To understand better this point, we carried out DFT calculations by reproducing the grain boundaries between the perovskite structure and the RPP. First, we built a $CsPbBr_2Cl$ NC composed of a 4 × 4 × 7 cubic unit cell (which corresponds to 2.6 × 2.6 × 4.3 nm). In this structure, each lead halide octahedron is formed equatorially by four bromide ions and axially by two chlorine atoms, which is in line with a 2:1 stoichiometric Br/Cl ratio (the actual ratio in the finite model system is about 1.5:1). From this structure, we formed the RPP interface by removing one layer of PbX_2 along the [100] direction, as is depicted in Figure 5a. All halide atoms at the RPP boundary were then replaced by iodine, while the CsI units at this interface were shifted half a unit cell in the *x* and *y* directions to resemble the RPP planes. The final elemental ratio for the RPP model system is 1.7:1.0:0.5, which is qualitatively in alignment with the EDS measurements.

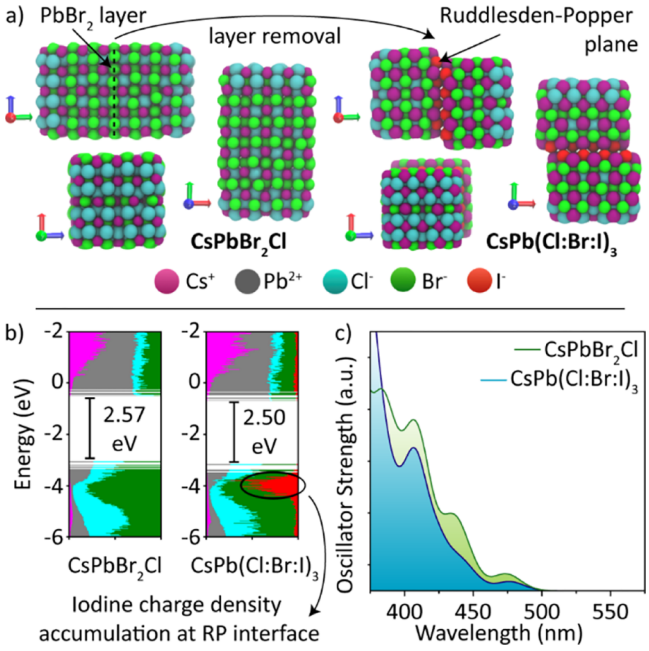

Figure 5. DFT studies performed on the $CsPbBr_2Cl$ and $CsPb(Cl:Br:I)_3$ NCs. (a) Relaxed $CsPbBr_2Cl$ structures (left) and $CsPb(Cl:Br:I)_3$ structures (right) shown from different directions and computed at the DFT/PBE levels of theory. (b) Electronic structure near the conduction and valence band regions. Each molecular orbital is decomposed in terms of atomic type contributions and is highlighted in a different color. (c) Absorption spectrum of each system computed using the simplified time-dependent (TDDFT/PBE) methodology.

We relaxed both of the structures and calculated the density of states (Figure 5b,c). We found that the band gap of each system is free of localized (trap) states, but there is a significant difference in the electronic structure near the valence band edge in the triple halide system. Here, the molecular orbitals (states) are predominantly composed of the *np* orbitals of the halides; however, the contribution of the iodine 5p orbitals at the RPP planes is not at the band edge but few hundredths

DOI: 10.1021/acs.chemmater.9b00489
Chem. Mater. 2019, 31, 2182−2190

meV below. This behavior is surprising because the iodine orbitals are expected to contribute at higher energies compared to the other halides. This effect, however, can be explained by the lack of the PbX_2 layer at the RPP interface that breaks the connection between the corner edge octahedra, lifting their electronic connection. This tells us that the interface resembles rather a wide band gap CsI structure, with the iodine orbitals pushed below the valence band edge.[49] This configuration, however, discards the idea that the segregation of iodine at the RPP interface alone localizes the hole carrier at the RPP interface, reducing the electron−hole overlap, and thus the emission efficiency. A most likely explanation to the loss of PLQY is that the RPP interface itself is defective, presumably due to some halide vacancies, which could form deep traps in the core region of the NCs that cannot be directly accessed postsynthetically via a surface treatment.

We also computed the optical spectrum of the $CsPbBr_2Cl$ and $CsPb(Cl:Br:I)_3$ NCs at a time-dependent DFT level of theory, analyzing the lowest 700 electronically excited states (Figure 5c). This revealed that the triple halide system maintains excitonic features in the band gap region, which is in agreement with our experiments.

To understand how the presence of the three types of halide atoms at different locations in the perovskite lattice can lead to iodine segregation at the RPP interface, we studied several isomeric $CsPb(Cl:Br:I)_3$ NC structures with equal amounts of the three halogen atoms with DFT. First, we designed a symmetric NC which was built from a $CsPb(Cl:Br:I)_3$ unit cell that was replicated evenly along the three axes by 2 unit cells (the size of the NC was about 3 nm). Using this configuration as a point of reference, we then swapped, for example, the chloride ions at the surface with the iodide ions that are present in the core so as to provide a qualitative picture of the diffusion of this latter ion type to the surface. The difference in the total energy of this structure compared to the one used as a point of reference provides us with a rough estimate of the likelihood that segregation will occur. An inspection of the DFT data shows that the segregation of iodide ions into the surface leads to an overall stabilization with respect to the symmetrical system by about 232 kcal/mol. This corresponds to about 3.7 kcal/mol for each Cl−I ion that has been swapped (in total, 62 were swapped). The inverse process, that is the diffusion of Cl ions to the surface, is energetically disfavored by about 121 kcal/mol, that is, 1.95 kcal/mol per swapped halide.

We also analyzed the segregation of Br with I and I with Cl, as is illustrated in Figure S14. The overall trend is that smaller ions prefer to be located at the core of the NC, while heavier ions prefer the surface. Although this result is only qualitative, it provides some insight as to how halide ions might be distributed in mixed lead halide NCs, especially in those that contain ions of very different sizes. In particular, these results show that iodine and chlorine have the lowest miscibility and that iodine prefers to move toward the surface of the RPP interface rather than remain in the core of the NC. This analysis, together with the conclusion from the Kanatzidis group that $Cs_2PbI_2Cl_2$ is thermodynamically more favorable to form over $CsPbCl_3$ + Cs_4PbI_6 (as well as $CsPbI_3$ + Cs_4PbCl_6) or CsCl + $PbBr_2$ (as well as CsBr + $PbCl_2$),[20] confirms that iodide segregation in the triple halide mixed NCs toward RPP planes is indeed a thermodynamically driven process.

To summarize, we have synthesized lead halide-based NCs with two new halide compositions: $Cs_2PbI_2Cl_2$ and $CsPb(Cl:Br:I)_3$. The $Cs_2PbI_2Cl_2$ NCs crystallize in a RPP and are the first reported fully inorganic lead halide RPP NCs. The $CsPb(Cl:Br:I)_3$ NCs crystallize in a cubic LHP crystal structure, but each NC contains several RPP plane shifts. The presence of iodine in the $CsPb(Cl:Br:I)_3$ NCs, even in very small amounts, systematically produces the RPP type shifts because of its size difference with respect to the other halides in the structure. Thus, these ions migrate outward and fill the halide positions at the plane interfaces. This work thus expands the list of LHP NCs consisting of multiple anions, a list that is strongly limited by the structural constraints imposed by size differences between the different anions. These new types of lead halide NCs will deserve further scrutiny in terms of mechanism of their formation, optoelectronic properties, as well as their use in optoelectronic applications. For instance, the $Cs_2PbI_2Cl_2$ NCs, because of their incorporation of heavy iodide ions, should be suitable for alpha particle detection, but at the same time, unlike the classical iodide perovskites, they do not absorb much in the visible region of the spectrum.[20] Furthermore, the $Cs_2PbI_2Cl_2$ NCs could be the predecessors of other interesting RPP NCs, such as mixed halide−pseudo halide $Cs_2PbI_2(thiocyanate)_2$ NCs.[50] Although the reported NCs in this work exhibit low PLQYs, they could be exploited for photodetectors. Finally, the reported NCs in this work may act potential hosts for various dopant atoms, with emission properties that could be different from those of doped halide perovskite NCs.

■ ASSOCIATED CONTENT

Supporting Information

The Supporting Information is available free of charge on the ACS Publications website at DOI: 10.1021/acs.chemmater.9b00489.

Additional details including XRD patterns, TEM images, and PL and absorption spectra of $CsPbCl_3$ and $CsPbBr_2Cl$ NCs; PLE data from $Cs_2PbI_2Cl_2$ NCs; PLQY data on $CsPb(Cl:Br:I)_3$ and $CsPbBr_2Cl$ NCs; additional HAADF-STEM images and StatSTEM data; and surface treatment data from $CsPb(Cl:Br:I)_3$ and $CsPbBr_2Cl$ NCs (PDF)

■ AUTHOR INFORMATION

Corresponding Authors

*E-mail: iinfant76@gmail.com (I.I.).
*E-mail: sara.bals@uantwerpen.be (S.B.).
*E-mail: liberato.manna@iit.it (L.M.).

ORCID

Dmitry Baranov: 0000-0001-6439-8132
Ahmed L. Abdelhady: 0000-0002-6637-8853
Sara Bals: 0000-0002-4249-8017
Liberato Manna: 0000-0003-4386-7985

Notes

The authors declare no competing financial interest.

■ ACKNOWLEDGMENTS

Q.A.A. and L.M. acknowledge funding from the European Union Seventh Framework Programme under grant agreement no. 614897 (ERC Consolidator Grant "TRANS-NANO"). The work of D.B. was supported by the European Union's Horizon 2020 research and innovation programme under the Marie Sklodowska-Curie grant agreement no. 794560. E.B. and S.B. acknowledge funding from the Research Foundation Flanders

DOI: 10.1021/acs.chemmater.9b00489
Chem. Mater. 2019, 31, 2182−2190

(G.038116N, G.03691, and funding of a postdoctoral grant to E.B.). I.I. acknowledges The Netherlands Organization of Scientific Research (NWO) for financial support through the Innovational Research Incentive (Vidi) Scheme (grant no. 723.013.002). The computational work was carried out on the Dutch national e-infrastructure with the support of the SURF Cooperative.

REFERENCES

(1) Correa-Baena, J.-P.; Saliba, M.; Buonassisi, T.; Grätzel, M.; Abate, A.; Tress, W.; Hagfeldt, A. Promises and Challenges of Perovskite Solar Cells. *Science* **2017**, *358*, 739−744.

(2) Protesescu, L.; Yakunin, S.; Bodnarchuk, M. I.; Krieg, F.; Caputo, R.; Hendon, C. H.; Yang, R. X.; Walsh, A.; Kovalenko, M. V. Nanocrystals of Cesium Lead Halide Perovskites ($CsPbX_3$, X = Cl, Br, and I): Novel Optoelectronic Materials Showing Bright Emission with Wide Color Gamut. *Nano Lett.* **2015**, *15*, 3692−3696.

(3) Akkerman, Q. A.; Rainò, G.; Kovalenko, M. V.; Manna, L. Genesis, Challenges and Opportunities for Colloidal Lead Halide Perovskite Nanocrystals. *Nat. Mater.* **2018**, *17*, 394−405.

(4) Lignos, I.; Morad, V.; Shynkarenko, Y.; Bernasconi, C.; Maceiczyk, R. M.; Protesescu, L.; Bertolotti, F.; Kumar, S.; Ochsenbein, S. T.; Masciocchi, N.; Guagliardi, A.; Shih, C.-J.; Bodnarchuk, M. I.; deMello, A. J.; Kovalenko, M. V. Exploration of near-Infrared-Emissive Colloidal Multinary Lead Halide Perovskite Nanocrystals Using an Automated Microfluidic Platform. *ACS Nano* **2018**, *12*, 5504−5517.

(5) Protesescu, L.; Yakunin, S.; Kumar, S.; Bär, J.; Bertolotti, F.; Masciocchi, N.; Guagliardi, A.; Grotevent, M.; Shorubalko, I.; Bodnarchuk, M. I.; Shih, C.-J.; Kovalenko, M. V. Dismantling the "Red Wall" of Colloidal Perovskites: Highly Luminescent Formamidinium and Formamidinium−Cesium Lead Iodide Nanocrystals. *ACS Nano* **2017**, *11*, 3119−3134.

(6) Akkerman, Q. A.; Meggiolaro, D.; Dang, Z.; De Angelis, F.; Manna, L. Fluorescent Alloy $CsPb_xMn_{1-x}I_3$ Perovskite Nanocrystals with High Structural and Optical Stability. *ACS Energy Lett.* **2017**, *2*, 2183−2186.

(7) Guria, A. K.; Dutta, S. K.; Adhikari, S. D.; Pradhan, N. Doping Mn^{2+} in Lead Halide Perovskite Nanocrystals: Successes and Challenges. *ACS Energy Lett.* **2017**, *2*, 1014−1021.

(8) Bezinge, L.; Maceiczyk, R. M.; Lignos, I.; Kovalenko, M. V.; deMello, A. J. Pick a Color Maria: Adaptive Sampling Enables the Rapid Identification of Complex Perovskite Nanocrystal Compositions with Defined Emission Characteristics. *ACS Appl. Mater. Interfaces* **2018**, *10*, 18869−18878.

(9) Swarnkar, A.; Mir, W. J.; Nag, A. Can B-Site Doping or Alloying Improve Thermal- and Phase-Stability of All-Inorganic $CsPbX_3$ (X = Cl, Br, I) Perovskites? *ACS Energy Lett.* **2018**, *3*, 286−289.

(10) Yong, Z.-J.; Guo, S.-Q.; Ma, J.-P.; Zhang, J.-Y.; Li, Z.-Y.; Chen, Y.-M.; Zhang, B.-B.; Zhou, Y.; Shu, J.; Gu, J.-L.; Zheng, L.-R.; Bakr, O. M.; Sun, H.-T. Doping-Enhanced Short-Range Order of Perovskite Nanocrystals for near-Unity Violet Luminescence Quantum Yield. *J. Am. Chem. Soc.* **2018**, *140*, 9942−9951.

(11) Swarnkar, A.; Ravi, V. K.; Nag, A. Beyond Colloidal Cesium Lead Halide Perovskite Nanocrystals: Analogous Metal Halides and Doping. *ACS Energy Lett.* **2017**, *2*, 1089−1098.

(12) Lu, M.; Zhang, X.; Zhang, Y.; Guo, J.; Shen, X.; Yu, W. W.; Rogach, A. L. Simultaneous Strontium Doping and Chlorine Surface Passivation Improve Luminescence Intensity and Stability of $CsPbI_3$ Nanocrystals Enabling Efficient Light-Emitting Devices. *Adv. Mater.* **2018**, *30*, 1804691.

(13) Akkerman, Q. A.; D'Innocenzo, V.; Accornero, S.; Scarpellini, A.; Petrozza, A.; Prato, M.; Manna, L. Tuning the Optical Properties of Cesium Lead Halide Perovskite Nanocrystals by Anion Exchange Reactions. *J. Am. Chem. Soc.* **2015**, *137*, 10276−10281.

(14) Nedelcu, G.; Protesescu, L.; Yakunin, S.; Bodnarchuk, M. I.; Grotevent, M. J.; Kovalenko, M. V. Fast Anion-Exchange in Highly Luminescent Nanocrystals of Cesium Lead Halide Perovskites ($CsPbX_3$, X = Cl, Br, I). *Nano Lett.* **2015**, *15*, 5635−5640.

(15) Davis, N. J. L. K.; de la Peña, F. J.; Tabachnyk, M.; Richter, J. M.; Lamboll, R. D.; Booker, E. P.; Wisnivesky Rocca Rivarola, F.; Griffiths, J. T.; Ducati, C.; Menke, S. M.; Deschler, F.; Greenham, N. C. Photon Reabsorption in Mixed $CsPbCl_3$:$CsPbI_3$ Perovskite Nanocrystal Films for Light-Emitting Diodes. *J. Phys. Chem. C* **2017**, *121*, 3790−3796.

(16) Dastidar, S.; Egger, D. A.; Tan, L. Z.; Cromer, S. B.; Dillon, A. D.; Liu, S.; Kronik, L.; Rappe, A. M.; Fafarman, A. T. High Chloride Doping Levels Stabilize the Perovskite Phase of Cesium Lead Iodide. *Nano Lett.* **2016**, *16*, 3563−3570.

(17) Mondal, N.; De, A.; Samanta, A. Biexciton Generation and Dissociation Dynamics in Formamidinium- and Chloride-Doped Cesium Lead Iodide Perovskite Nanocrystals. *J. Phys. Chem. Lett.* **2018**, *9*, 3673−3679.

(18) Colella, S.; Mosconi, E.; Fedeli, P.; Listorti, A.; Gazza, F.; Orlandi, F.; Ferro, P.; Besagni, T.; Rizzo, A.; Calestani, G.; Gigli, G.; De Angelis, F.; Mosca, R. $MAPbI_{3-x}Cl_x$ Mixed Halide Perovskite for Hybrid Solar Cells: The Role of Chloride as Dopant on the Transport and Structural Properties. *Chem. Mater.* **2013**, *25*, 4613−4618.

(19) Suarez, B.; Gonzalez-Pedro, V.; Ripolles, T. S.; Sanchez, R. S.; Otero, L.; Mora-Sero, I. Recombination Study of Combined Halides (Cl, Br, I) Perovskite Solar Cells. *J. Phys. Chem. Lett.* **2014**, *5*, 1628−1635.

(20) Li, J.; Yu, Q.; He, Y.; Stoumpos, C. C.; Niu, G.; Trimarchi, G. G.; Guo, H.; Dong, G.; Wang, D.; Wang, L.; Kanatzidis, M. G. $Cs_2PbI_2Cl_2$, All-Inorganic Two-Dimensional Ruddlesden−Popper Mixed Halide Perovskite with Optoelectronic Response. *J. Am. Chem. Soc.* **2018**, *140*, 11085−11090.

(21) Almeida, G.; Goldoni, L.; Akkerman, Q.; Dang, Z.; Khan, A. H.; Marras, S.; Moreels, I.; Manna, L. Role of Acid-Base Equilibria in the Size, Shape, and Phase Control of Cesium Lead Bromide Nanocrystals. *ACS Nano* **2018**, *12*, 1704−1711.

(22) Akkerman, Q. A.; Park, S.; Radicchi, E.; Nunzi, F.; Mosconi, E.; De Angelis, F.; Brescia, R.; Rastogi, P.; Prato, M.; Manna, L. Nearly Monodisperse Insulator Cs_4PbX_6 (X = Cl, Br, I) Nanocrystals, Their Mixed Halide Compositions, and Their Transformation into $CsPbX_3$ Nanocrystals. *Nano Lett.* **2017**, *17*, 1924−1930.

(23) Akkerman, Q. A.; Martínez-Sarti, L.; Goldoni, L.; Imran, M.; Baranov, D.; Bolink, H. J.; Palazon, F.; Manna, L. Molecular Iodine for a General Synthesis of Binary and Ternary Inorganic and Hybrid Organic−Inorganic Iodide Nanocrystals. *Chem. Mater.* **2018**, *30*, 6915−6921.

(24) De Backer, A.; van den Bos, K. H. W.; Van den Broek, W.; Sijbers, J.; Van Aert, S. StatSTEM: An Efficient Approach for Accurate and Precise Model-Based Quantification of Atomic Resolution Electron Microscopy Images. *Ultramicroscopy* **2016**, *171*, 104−116.

(25) Hutter, J.; Iannuzzi, M.; Schiffmann, F.; VandeVondele, J. $_{CP}2_K$: Atomistic Simulations of Condensed Matter Systems. *Wiley Interdiscip. Rev.: Comput. Mol. Sci.* **2014**, *4*, 15−25.

(26) Perdew, J. P.; Burke, K.; Ernzerhof, M. Generalized Gradient Approximation Made Simple. *Phys. Rev. Lett.* **1996**, *77*, 3865−3868.

(27) VandeVondele, J.; Hutter, J. Gaussian Basis Sets for Accurate Calculations on Molecular Systems in Gas and Condensed Phases. *J. Chem. Phys.* **2007**, *127*, 114105.

(28) ten Brinck, S.; Infante, I. Surface Termination, Morphology, and Bright Photoluminescence of Cesium Lead Halide Perovskite Nanocrystals. *ACS Energy Lett.* **2016**, *1*, 1266−1272.

(29) Giansante, C.; Infante, I. Surface Traps in Colloidal Quantum Dots: A Combined Experimental and Theoretical Perspective. *J. Phys. Chem. Lett.* **2017**, *8*, 5209−5215.

(30) Bodnarchuk, M. I.; Boehme, S. C.; ten Brinck, S.; Bernasconi, C.; Shynkarenko, Y.; Krieg, F.; Widmer, R.; Aeschlimann, B.; Günther, D.; Kovalenko, M. V.; Infante, I. Rationalizing and Controlling the Surface Structure and Electronic Passivation of Cesium Lead Halide Nanocrystals. *ACS Energy Lett.* **2019**, *4*, 63−74.

DOI: 10.1021/acs.chemmater.9b00489
Chem. Mater. 2019, 31, 2182−2190

(31) Grimme, S. A Simplified Tamm-Dancoff Density Functional Approach for the Electronic Excitation Spectra of Very Large Molecules. *J. Chem. Phys.* **2013**, *138*, 244104.
(32) Zapata, F.; Infante, I. QMWorks-NAMD. *Zenodo* **2017**, DOI: 10.5281/zenodo.1051030.
(33) Vashishtha, P.; Ng, M.; Shivarudraiah, S. B.; Halpert, J. E. High Efficiency Blue and Green Light-Emitting Diodes Using Ruddlesden−Popper Inorganic Mixed Halide Perovskites with Butylammonium Interlayers. *Chem. Mater.* **2019**, *31*, 83−89.
(34) Chang, Y.-H.; Lin, J.-C.; Chen, Y.-C.; Kuo, T.-R.; Wang, D.-Y. Facile Synthesis of Two-Dimensional Ruddlesden−Popper Perovskite Quantum Dots with Fine-Tunable Optical Properties. *Nanoscale Res. Lett.* **2018**, *13*, 247.
(35) Blancon, J.-C.; Tsai, H.; Nie, W.; Stoumpos, C. C.; Pedesseau, L.; Katan, C.; Kepenekian, M.; Soe, C. M. M.; Appavoo, K.; Sfeir, M. Y.; Tretiak, S.; Ajayan, P. M.; Kanatzidis, M. G.; Even, J.; Crochet, J. J.; Mohite, A. D. Extremely Efficient Internal Exciton Dissociation through Edge States in Layered 2D Perovskites. *Science* **2017**, *355*, 1288−1292.
(36) Tsai, H.; Nie, W.; Blancon, J.-C.; Stoumpos, C. C.; Asadpour, R.; Harutyunyan, B.; Neukirch, A. J.; Verduzco, R.; Crochet, J. J.; Tretiak, S.; Pedesseau, L.; Even, J.; Alam, M. A.; Gupta, G.; Lou, J.; Ajayan, P. M.; Bedzyk, M. J.; Kanatzidis, M. G.; Mohite, A. D. High-Efficiency Two-Dimensional Ruddlesden−Popper Perovskite Solar Cells. *Nature* **2016**, *536*, 312−316.
(37) Weidman, M. C.; Goodman, A. J.; Tisdale, W. A. Colloidal Halide Perovskite Nanoplatelets: An Exciting New Class of Semiconductor Nanomaterials. *Chem. Mater.* **2017**, *29*, 5019−5030.
(38) Weidman, M. C.; Seitz, M.; Stranks, S. D.; Tisdale, W. A. Highly Tunable Colloidal Perovskite Nanoplatelets through Variable Cation, Metal, and Halide Composition. *ACS Nano* **2016**, *10*, 7830−7839.
(39) Akkerman, Q. A.; Motti, S. G.; Srimath Kandada, A. R.; Mosconi, E.; D'Innocenzo, V.; Bertoni, G.; Marras, S.; Kamino, B. A.; Miranda, L.; De Angelis, F.; Petrozza, A.; Prato, M.; Manna, L. Solution Synthesis Approach to Colloidal Cesium Lead Halide Perovskite Nanoplatelets with Monolayer-Level Thickness Control. *J. Am. Chem. Soc.* **2016**, *138*, 1010−1016.
(40) Tyagi, P.; Arveson, S. M.; Tisdale, W. A. Colloidal Organohalide Perovskite Nanoplatelets Exhibiting Quantum Confinement. *J. Phys. Chem. Lett.* **2015**, *6*, 1911−1916.
(41) Yu, Y.; Zhang, D.; Yang, P. Ruddlesden−Popper Phase in Two-Dimensional Inorganic Halide Perovskites: A Plausible Model and the Supporting Observations. *Nano Lett.* **2017**, *17*, 5489−5494.
(42) Ahmed, T.; Seth, S.; Samanta, A. Boosting the Photoluminescence of $CsPbX_3$ (X = Cl, Br, I) Perovskite Nanocrystals Covering a Wide Wavelength Range by Postsynthetic Treatment with Tetrafluoroborate Salts. *Chem. Mater.* **2018**, *30*, 3633−3637.
(43) Stoumpos, C. C.; Cao, D. H.; Clark, D. J.; Young, J.; Rondinelli, J. M.; Jang, J. I.; Hupp, J. T.; Kanatzidis, M. G. Ruddlesden−Popper Hybrid Lead Iodide Perovskite 2D Homologous Semiconductors. *Chem. Mater.* **2016**, *28*, 2852−2867.
(44) Morrell, M. V.; He, X.; Luo, G.; Thind, A. S.; White, T. A.; Hachtel, J. A.; Borisevich, A. Y.; Idrobo, J.-C.; Mishra, R.; Xing, Y. Significantly Enhanced Emission Stability of $CsPbBr_3$ Nanocrystals Via Chemically Induced Fusion Growth for Optoelectronic Devices. *ACS Appl. Nano Mater.* **2018**, *1*, 6091−6098.
(45) Thind, A. S.; Luo, G.; Hachtel, J. A.; Morrell, M. V.; Cho, S. B.; Borisevich, A. Y.; Idrobo, J. C.; Xing, Y.; Mishra, R. Atomic Structure and Electrical Activity of Grain Boundaries and Ruddlesden-Popper Faults in Cesium Lead Bromide Perovskite. *Adv. Mater.* **2019**, *31*, No. e1805047.
(46) Koscher, B. A.; Swabeck, J. K.; Bronstein, N. D.; Alivisatos, A. P. Essentially Trap-Free $CsPbBr_3$ Colloidal Nanocrystals by Postsynthetic Thiocyanate Surface Treatment. *J. Am. Chem. Soc.* **2017**, *139*, 6566−6569.
(47) Almeida, G.; Ashton, O. J.; Goldoni, L.; Maggioni, D.; Petralanda, U.; Mishra, N.; Akkerman, Q. A.; Infante, I.; Snaith, H. J.; Manna, L. The Phosphine Oxide Route toward Lead Halide Perovskite Nanocrystals. *J. Am. Chem. Soc.* **2018**, *140*, 14878−14886.
(48) Li, F.; Liu, Y.; Wang, H.; Zhan, Q.; Liu, Q.; Xia, Z. Postsynthetic Surface Trap Removal of $CsPbX_3$ (X = Cl, Br, or I) Quantum Dots Via a ZnX_2/Hexane Solution toward an Enhanced Luminescence Quantum Yield. *Chem. Mater.* **2018**, *30*, 8546−8554.
(49) McKenna, K. P. Electronic Properties of {111} Twin Boundaries in a Mixed-Ion Lead Halide Perovskite Solar Absorber. *ACS Energy Lett.* **2018**, *3*, 2663−2668.
(50) Numata, Y.; Sanehira, Y.; Ishikawa, R.; Shirai, H.; Miyasaka, T. Thiocyanate Containing Two-Dimensional Cesium Lead Iodide Perovskite, $Cs_2PbI_2(SCN)_2$: Characterization, Photovoltaic Application, and Degradation Mechanism. *ACS Appl. Mater. Interfaces* **2018**, *10*, 42363−42371.

DOI: 10.1021/acs.chemmater.9b00489
Chem. Mater. 2019, 31, 2182−2190